Nonlinear dynamics of in-plane ring resonator for mass sensing

Azizi, Saber; Madinei, Hadi; Khodaparast, Hamed Haddad; Steeneken, Peter; Younis, Mohammad I.; Rezazadeh, Ghader

DOI
10.1007/s00542-025-05960-8

Publication date
2025

Document Version
Final published version

Published in
Microsystem Technologies

Microsystem Technologies (2025) 31:3945–3957
https://doi.org/10.1007/s00542-025-05960-8

TECHNICAL PAPER

Nonlinear dynamics of in-plane ring resonator for mass sensing

Saber Azizi[1] · Hadi Madinei[1] · Hamed Haddad Khodaparast[1] · Peter Steeneken[2] · Mohammad I. Younis[3] · Ghader Rezazadeh[4,5]

Received: 25 March 2025 / Accepted: 15 September 2025 / Published online: 21 October 2025

Abstract
Mass sensing using MEMS is crucial for detecting minute changes in mass with high sensitivity, enabling applications in environmental monitoring, medical diagnostics, and chemical detection. However, fluid damping in these environments is relatively high and can lead to reduction of the quality factor and sensitivity of these sensors. In this paper, we present a rotating ring resonator for mass sensing applications and investigate its nonlinear dynamics and bifurcation. The ring is supported by four slender beams and subjected to rotational base excitation. The shift in the nonlinear bifurcation point on the frequency response curve is used for mass sensing, which is significant because the device exhibits multiple nonlinear bifurcation points. The structure is designed and modelled to vibrate in a rotational in-plane mode, to provide lower damping and higher quality factor compared to cantilever-based mass sensors that operate in a translational out-of-plane mode. Moreover, the structure exhibits nonlinear resonance zones within the super harmonic regime, enabling mass detection at a particular fraction of the primary resonance zone. At lower excitation amplitudes, the linear response dominates, and the device also allows mass detection in the linear regime via resonance frequency shifts.

1 Introduction

Over the past decades, there has been a steadily growing demand for the application of microelectromechanical systems (MEMS) (Pasquale and Somà 2010; Azizi et al. 2023; Zamanzadeh et al. 2020). MEMS sensors and actuators benefit from low weight, low fabrication costs, and high sensitivity, which are critically important in high-tech biomedical applications (Yaqoob et al. 2022). Among MEMS sensors and actuators, mass sensors have garnered significant attention for their ability to detect the masses of viruses and biomarkers for disease detection applications (Alneamy and Ouakad 2023; Jingjing, et al. 2016; Alvarez and Lechuga 2010). Measuring extremely small masses in biomedical contexts, such as viruses, bacteria, biomolecules, DNA, or proteins, has always posed significant challenges (Baguet et al. 2019; Chauhan and Ansari 2021; Mohammad 2011; Katzis et al. 2022; Hashoul and Haick 2019). Various sensing mechanisms have been utilised so far for the capturing of the bio masses which include resonance frequency shifts (Park et al. 2012; Chellasivalingam et al. 2020; Joshi et al. 2019), bifurcation based switching (Azizi et al. 2023; Alneamy and Ouakad 2023; Meesala et al. 2020; Nayfeh et al. 2010; Kumar et al. 2011; Yuksel et al. 2019) and symmetry-breaking (Baguet et al. 2019; Chellasivalingam et al. 2020). In terms of sensing mechanisms, the most commonly used ones include piezoelectric (Chellasivalingam et al. 2020; Joshi et al. 2019; Azizi et al. 2017; Kumar, et al. 2011; Xu and Yan 2024; Toledo et al. 2019), electrostatic (Baguet et al. 2019; Elliott et al. 2017; Botamanenko et al. 2023), and magnetic detection (Jafari et al. 2017; Timurdogan et al. 2011). Though bifurcation based sensors have been addressed in the literature to measure mass there are some complications regarding the application of phase-locked loops (PLL), to address this issue, Yuksel et al. (2019)

✉ Saber Azizi
saber.azizi@swansea.ac.uk

1 Aerospace department, Faculty of Science and Engineering, Swansea University, Swansea, UK

2 Department of Precision and Microsystems Engineering, Delft University of Technology, Delft, Netherlands

3 Department of Mechanical Engineering, State University of New York, Binghamton, USA

4 Centre for Materials Technologies, Skolkovo Institute of Science and Technology, Moscow, Russia

5 Mechanical Engineering Department, Faculty of Engineering, Urmia University, 11km Sero Road, Urmia 16557153, Iran

introduced a trajectory-locked loop (TLL) architecture to enable stable mass sensing in the nonlinear regime of Duffing resonators. In this method, the system avoids locking to a fixed phase instead, it continuously circulates within the hysteresis window, alternating between the jump frequencies f_{up} and f_{down}. This approach allows for rapid and sensitive tracking of frequency shifts induced by single particle events, even beyond the linear dynamic range of the sensor.

MEMS mass sensors have been utilized in the diagnosis of various diseases to date. Timurdogan et al. applied resonant microcantilever arrays (Timurdogan et al. 2011), functionalised with Hepatitis antibodies. They detected both Hepatitis *A* and Hepatitis *C* antigens. Shafiee et al. (Shafiee et al. 2013), detected HIV virus through label-free electrical sensing of viral nano-lysate. Chen et al. (Li et al. 2019) developed a microcantilever array biosensor for simultaneously measuring two biomarkers carcinoembryonic antigen (CEA) and α-fetoprotein (AFP) by means of an optical readout technique. One of the challenges of cantilever beam sensors is that their stiffness is influenced by the thickness and the position of the mass of the antigen or biomarker deposited on the beam. This absorption-induced stiffness can lead to errors in mass detection (Jingjing et al. 2016; Alvarez and Lechuga 2010; Johnson and Mutharasan 2012; Lee et al. 2004). Wang et al. (Jingjing, et al. 2016) developed a cantilever based sensor for the detection of the biomarkers of liver cancer with various concentrations of AFP. They reported a huge frequency shift of 830 Hz due to absorption induced stiffness which was two orders of magnitude larger than the theoretical calculations. To address the challenge of absorption induced stiffness, they designed a micro-cavity at the free end of the cantilever beams for local antibody immobilization and as a result reduced the absorption induced stiffness of the system. A similar approach was taken by Wang et al. (2015), to reduce the absorption induced stiffness of a the arrays of cantilever beams. Stachiv al. (2022) reported on the challenges posed by size and absorption-induced stiffness in cantilever-based sensors. In another study Stachiv et al. (2020) demonstrated that for heavy analytes ($>MDa$), conventional multimode frequency shift methods yield inaccurate mass estimates. They proposed a technique based on monitoring Q-factor changes in air, eliminating the need to resolve analyte position or stiffness. Their method showed highest sensitivity using lateral modes and enabled accurate mass detection of large biomolecules and cells. Cantilever-based mass sensors have also been used to measure volatile organic compounds (VOCs) in exhaled breath (Kurmendra and R. Kumar 2019; Gupta et al. 2018). However, the challenges of dependency and absorption-induced stiffness remain significant. Biosensing applications require the sensor to be used in air and liquid environment (Johnson and Mutharasan 2012). Another challenge in the application of cantilever-based bio medical mass sensors is the high damping ratio and accordingly low quality factor which is mainly due to the out of plane motion of the cantilever beam (Timurdogan et al. 2011; Azizi et al. 2012; Hansen and Thundat 2005), especially position when it is operated in liquid; Various methods have been proposed to address the challenge of high damping ratio involved in bio mass detection; these include the so called “dip & dry” method (Timurdogan et al. 2011) which brings about other implications working with activated microbes, wetting, and change in stiffness due to surface adhesion (Gfeller et al. 2005). Lee et al. (2011) designed microchannel inside the cantilever beams to allow the liquid to pass through; although the method was a novel approach but was able to pass very small sample volumes. Olcum et al. (2014) designed and fabricated a nano resonator based on cantilever structure to detect self-assembled DNA nano particles. Some investigations have been carried out to operate cantilever-based mass sensors in higher resonant modes to decrease the associated damping ratio. Higher modes result in increased stiffness, reduced damping ratios, and, consequently, a higher quality factor (Johnson and Mutharasan 2012; Maraldo and Mutharasan 2007);

As discussed, despite their popularity in biomass sensing, cantilever-based biomass sensors face two main challenges: absorption-induced stiffness and high damping ratios due to out-of-plane motion. To reduce damping, and increase Q-factor, it is beneficial to minimize the amount of liquid that needs to be displaced. To achieve this operation mode, we propose a rotational ring biomass sensor featuring a ring-based structure supported by four clamped–clamped microbeams. This model is expected to benefit from a significantly low damping ratio due to the in-plane nature of the motion. The advantage of the middle ring over the disc is that it minimizes the impact of position-dependent added mass on the dynamics of the central disc. The biomass is assumed to be deposited on the central ring, which is relatively thin in comparison to the overall structure. The model minimises absorption-induced stiffness and exhibits significantly reduced damping due to in-plane motion (Azizi et al. 2012). The frequency response curves are derived using the continuation technique, and the bifurcation points are identified. To verify the continuation approach, the frequency response curves in the vicinity of the first two primary resonances are derived based on multiple time scales method. The system is designed to operate near the catastrophic bifurcation points (Nayfeh and Balachandran 2008), such that biomass deposition triggers the bifurcation, enabling biomass detection. The designed system targets measuring bio masses in the order of picograms which is ideal for the detection of the biomarkers of variety of cancers including liver (AFP), Prostate (PSA) and Lung cancer (CA-125).

2 Modelling

The model we have investigated, benefits from in-plane motion, which helps to address the significant damping typically observed in cantilever-based mass sensors due to their out-of-plane motion. The schematics of the model which consists of a ring-based mass along with the supporting beams are illustrated in Fig. 1. The supporting beams, which contribute torsional stiffness to the central ring (as shown in the first two mode shapes in Fig. 1), are connected at one end to the central ring and at the other end to the fully fixed substrate. The outer and inner radii of the central ring are denoted by R and R_i respectively. The supporting beams have length l_s, thickness h, and width of t_s. The substrate is assumed to be rigid and is mounted on top of a motion-controlled base, which applies harmonic excitation in the form of $\theta(t) = \theta_0 \sin(\omega t)$. The coordinate system $x_s - y_s$ is attached to the left end of the support beam. The material has a density ρ and Young's modulus E. The coordinate system x–y is attached to the centre of the ring and rotates with it.

Considering inertial coordinate system x–y with unit vectors (***i-j***) which is attached to the centre of the ring, the position vector $\overrightarrow{R}_p$ of a point 'p' on the support beam can be expressed in the form of Eq. (1).

$$\overrightarrow{R}_p = (-R_o + x_s)\,\boldsymbol{i} + w_s \boldsymbol{j} \tag{1}$$

Considering the harmonic base excitation $\theta(t)$, the velocity of point 'p' is in the following form (Azizi et al. 2012):

$$\dot{\overrightarrow{R}}_p = -\dot{\theta} w_s \boldsymbol{i} + \left(\dot{w}_s + \dot{\theta}\,(-R_o + x_s)\right)\boldsymbol{j} \tag{2}$$

Considering Eq. (2) The kinetic energy of the system can be expressed in the following form (Azizi et al. 2023; Azizi et al. 2017; Azizi et al. 2022):

$$T = \tfrac{1}{2}(\rho A)_s\, n_s \int_0^{l_s} \left((-\dot{\theta} w_s)^2 + \left(\dot{w}_s + \dot{\theta}\,(-R_o + x_s)\right)^2\right) dx_s + \tfrac{1}{2} I_D \left(\dot{\varphi} + \dot{\theta}\right)^2 \tag{3}$$

Where I_D represents the mass moment of inertia of the disc and the added mass about the centre of the disc, $\dot{\varphi}$ denotes the angular velocity of the disc relative to the base and n_s is the number of support beams. Considering the assumption of the stretching effect and neglecting the longitudinal inertia (Nayfeh and P.F.P., 2004; Azizi et al. 2014), The potential

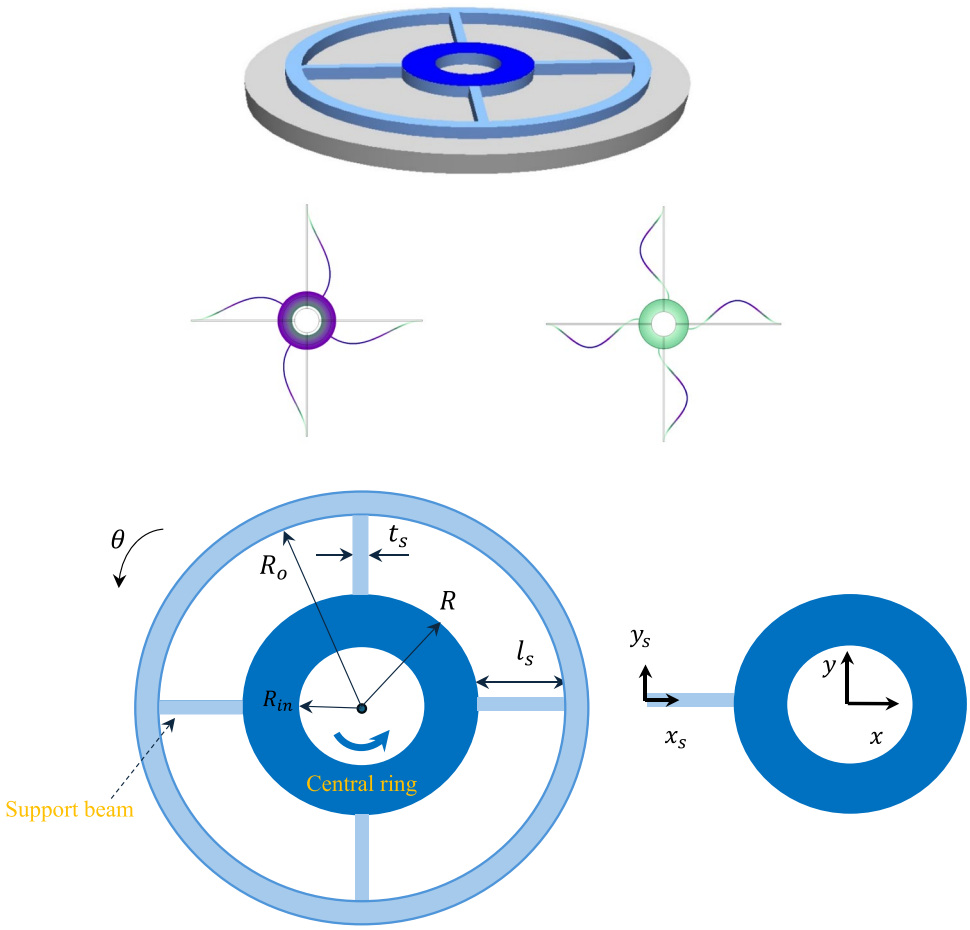

Fig. 1 Schematics of the ring and the support beam subjected to base excitation, with the first two mode shapes included (by COMSOL)

energy of the support beams is expressed in the following form:

$$U = \frac{1}{2}(EI)_s n_s \int_0^{l_s} w_s''^2 dx_s + \frac{EA}{8l_s} n_s \left(\int_0^{l_s} w_s'^2 dx_s \right)^2 \tag{4}$$

Where, I and A are the second moment of inertia about the neutral axis and the cross-sectional area of the support beams. Assuming the solution to be in the form of $w_s(x_s,t) = \sum_i^n q_i(t)\,\psi_{s_i}(x_s)$ (Rashidi et al. 2024, 2023), where $q_i(t)$ and $\psi_{s_i}(x_s)$ are the generalised coordinates and the mode shapes which satisfy the boundary conditions associated with the support beams, the kinetic and the potential energies reduce to:

$$\begin{aligned} T = {} & \tfrac{1}{2}(\rho A)_s n_s \Big(\dot\theta^2 \textstyle\sum_{i=1}^n \sum_{j=1}^n q_i(t)\,q_j(t) \int_0^{l_s} \psi_{s_i}(x_s)\psi_{s_j}(x_s)dx_s \\ & + \textstyle\sum_{i=1}^n \sum_{j=1}^n \dot q_i(t)\,\dot q_j(t) \int_0^{l_s} \psi_{s_i}(x_s)\,\psi_{s_j}(x_s)\,dx_s \\ & + \dot\theta^2 \textstyle\int_0^{l_s} (R_o - x_s)^2\,dx_s \\ & - 2\dot\theta \textstyle\sum_{i=1}^n \dot q_i(t) \int_0^{l_s} (R_o - x_s)\,\psi_{s_i}(x_s)dx_s \Big) \\ & + \tfrac{1}{2} I_D \left(\sum_{i=1}^n \sum_{j=1}^n \dot q_i(t)\,\dot q_j(t)\,\psi'_{s_i}(l_s)\,\psi'_{s_j}(l_s) + \dot\theta^2 \right. \\ & \left. + 2\dot\theta \sum_{i=1}^n \dot q_i(t) \right) \end{aligned} \tag{5}$$

$$\begin{aligned} U = {} & \tfrac{1}{2}(EI)_s n_s \left(\sum_{i=1}^n \sum_{j=1}^n q_i(t)\,q_j(t) \int_0^{l_s} \psi''_{s_i}(x_s)\,\psi''_{s_j}(x_s)\,dx_s \right) \\ & + \tfrac{EA}{8l_s} n_s \left(\sum_{i=1}^n \sum_{j=1}^n \sum_{k=1}^n \sum_{o=1}^n q_i(t)\,q_j(t)\,q_k(t)\,q_o(t) \right. \\ & \left. \times \int_0^{l_s} \psi'_{s_i}(x_s)\,\psi'_{s_j}(x_s)\,dx_s \int_0^{l_s} \psi'_{s_k}(x_s)\,\psi'_{s_o}(x_s)\,dx_s \right) \end{aligned}$$

The derivation process of the associated shape functions is given in appendix 1. In Eq. (5) the angular velocity of the central ring with respect to the base ($\dot\varphi$), has been approximated by $\sum_{i=1}^n \psi'_{s_i}(l_s)\,\dot q_i(t)$ which is the gradient of the support beams at $x_s = l_s$.

To account for the effect of the dissipation on the motion equations, the Rayleigh's dissipation function is defined as follows (Mohammad and Y., 2011):

$$R_D = \frac{1}{2} c_s n_s \int_0^{l_s} \left(\frac{\partial w_s}{\partial t} \right)^2 dx_s \tag{6}$$

Where, c_s is the damping coefficient per unit length of the support beam. Considering the non-dimensionalising parameters T_t, g and Θ the non-dimensional parameters $\widehat{t}$, $\widehat{w}_s$ and $\widehat{\theta}$ are defined in the following form.

$$\widehat{t} = \frac{t}{T_t} \widehat{w}_s = \frac{w_s}{g} \widehat{\theta} = \frac{\theta}{\Theta} \tag{7}$$

For simplicity the over hats have been removed in the rest of the paper. Introducing Eq. (7) to the Lagrangian function ($L = T - U$) (Azizi et al. 2023; Firoozy et al. 2017), and considering the contribution of the first two modes in the solution, the equations of the motion reduce to:

$$\begin{aligned} & M_1\ddot q_1 + M_2\ddot q_2 + Kl_1 q_1 + Kl_2 q_2 + Kn_1 q_1^3 + Kn_2 q_2^3 \\ & + Kg_1 q_1 q_2^2 + Kg_2 q_2 q_1^2 + C_1\dot q_1 + C_2\dot q_2 = F_1 \\ & M_2\ddot q_1 + M_3\ddot q_2 + Kl_2 q_1 + Kl_3 q_2 + Kn_3 q_1^3 + Kn_4 q_2^3 \\ & + Kg_3 q_1 q_2^2 + Kg_4 q_2 q_1^2 + C_2\dot q_1 + C_3\dot q_2 = F_2 \end{aligned} \tag{8}$$

Where constants in Eq. (8) have been introduced in Appendix 2.

To apply multiple time scales (MTS) as a well-known perturbation based method, the bookkeeping parameter ε is introduced to keep track of the order of the nonlinear terms in the motion equations (Nayfeh 1981); this has been carried out as follows:

$$\begin{aligned} & M_1\ddot q_1 + M_2\ddot q_2 + Kl_1 q_1 + Kl_2 q_2 \\ & + \varepsilon\left(Kn_1 q_1^3 + Kn_2 q_2^3 + Kg_1 q_1 q_2^2 + Kg_2 q_2 q_1^2 + C_1\dot q_1 + C_2\dot q_2 \right) = \varepsilon F_1 \\ & M_2\ddot q_1 + M_3\ddot q_2 + Kl_2 q_1 + Kl_3 q_2 + \varepsilon\left(Kn_3 q_1^3 + Kn_4 q_2^3 \right. \\ & \left. + Kg_3 q_1 q_2^2 + Kg_4 q_2 q_1^2 + C_2\dot q_1 + C_3\dot q_2 \right) = \varepsilon F_2 \end{aligned} \tag{9}$$

To enable the investigation of primary resonance, the excitation forces must be of an order of magnitude less than those in the linear problem; otherwise, they will not appear in the solvability condition of the first order. This does not imply that primary resonance will not occur otherwise, but it guarantees that the conditions of the appearance of primary resonance are met. Assuming the asymptotic solution for q_1 and q_2 to be in the following form:

$$\begin{aligned} q_1(T_0,T_1) &= u_0(T_0,T_1) + \varepsilon u_1(T_0,T_1) + \mathrm{O}(\varepsilon^2) \\ q_2(T_0,T_1) &= v_0(T_0,T_1) + \varepsilon v_1(T_0,T_1) + \mathrm{O}(\varepsilon^2) \end{aligned} \tag{10}$$

where, $T_0 = t$, $T_1 = \varepsilon t$ are fast and slow time scales respectively. Substituting the asymptotic solutions in Eq. (10), considering $D_n = \frac{\partial}{\partial T_n}$, and equating coefficients of like powers of ε we conclude:

$$\varepsilon^0 : M_1 D_0^2 u_0 + M_2 D_0^2 v_0 + Kl_1 u_0 + Kl_2 v_0 = 0 \tag{11}$$

$$M_2 D_0^2 u_0 + M_3 D_0^2 v_0 + Kl_2 u_0 + Kl_3 v_0 = 0$$

$$\begin{aligned} & \varepsilon^1 : M_1 D_0^2 u_1 + M_2 D_0^2 v_1 + Kl_1 u_1 + Kl_2 v_1 \\ & = -2M_1 D_0 D_1 u_0 - 2M_2 D_0 D_1 v_0 - Kn_1 u_0^3 - Kn_2 v_0^3 - Kg_1 u_0 v_0^2 \\ & - Kg_2 v_0 u_0^2 - C_1\dot u_1 - C_2\dot v_1 + F_1 \end{aligned}$$

$$M_2D_0^2u_1 + M_3D_0^2v_1 + Kl_2u_1 + Kl_3v_1 = -2M_2D_0D_1u_0 - 2M_3D_0D_1v_0 - Kn_3u_0^3 - Kn_4v_0^3 - Kg_3u_0v_0^2 - Kg_4v_0u_0^2 - C_2\dot{u}_1 - C_3\dot{v}_1 + F_2$$

The solution to order ε^0 Eq. (12) is expressed in the following form:

$$\begin{Bmatrix} u_0(T_0,T_1) \\ v_0(T_0,T_1) \end{Bmatrix} = \begin{bmatrix} 1 & -0.19 \\ 0.04 & 0.98 \end{bmatrix} \begin{Bmatrix} A(T_1)e^{i\omega_{n_1}T_0} \\ B(T_1)e^{i\omega_{n_2}T_0} \end{Bmatrix} + CC \quad (12)$$

In Eq. (12), the modal matrix is derived from the coupled linear free vibration problem. $A(T_1)$ and $B(T_1)$ are undetermined at this level of approximation; they are determined at the next level by imposing the solvability condition. Substituting Eq. (12), in the order ε^1 Eq. (11), and expressing the forcing terms in $F_1 = f_1\frac{1}{2}\left(e^{i\Omega T_0} + e^{-i\Omega T_0}\right)$, $F_2 = f_2\frac{1}{2}\left(e^{i\Omega T_0} + e^{-i\Omega T_0}\right)$ and seeking a particular solution free of secular terms in the form of:

$$\begin{Bmatrix} u_0 \\ v_0 \end{Bmatrix} = \begin{bmatrix} Q_1(T_1) & Q_2(T_1) \\ P_1(T_1) & P_2(T_1) \end{bmatrix} \begin{Bmatrix} e^{i\omega_{n_1}T_0} \\ e^{i\omega_{n_2}T_0} \end{Bmatrix} + CC \quad (13)$$

Introducing Eq. (13), to Eq. (12), we obtain:

$$\begin{aligned} &\left[\left(-M_1\omega_{n_1^2} + Kl_1\right)Q_1 + \left(-M_2\omega_{n_1^2} + Kl_2\right)P_1\right]e^{i\omega_{n_1}T_0} \\ &+ \left[\left(-M_1\omega_{n_2^2} + Kl_1\right)Q_2 + \left(-M_2\omega_{n_2^2} + Kl_2\right)P_2\right]e^{i\omega_{n_2}T_0} \\ &= \chi_{11}e^{i\omega_{n_1}T_0} + \chi_{12}e^{i\omega_{n_2}T_0} \end{aligned}$$

$$\begin{aligned} &\left[\left(-M_2\omega_{n_1^2} + Kl_2\right)Q_1 + \left(-M_3\omega_{n_1^2} + Kl_3\right)P_1\right]e^{i\omega_{n_1}T_0} \\ &+ \left[\left(-M_2\omega_{n_2^2} + Kl_2\right)Q_2 + \left(-M_3\omega_{n_2^2} + Kl_3\right)P_2\right]e^{i\omega_{n_2}T_0} \\ &= \chi_{21}e^{i\omega_{n_1}T_0} + \chi_{22}e^{i\omega_{n_2}T_0} \end{aligned} \quad (14)$$

By equating the coefficients of each of $e^{i\omega_{n1}T_0}$ and $e^{i\omega_{n2}T_0}$ on both sides, we derive two sets of two inhomogeneous algebraic equations for Q_1 , P_1 andQ_2,P_2. As the homogenous part of the equations have a nontrivial solution, the solvability condition can be expressed as:

$$\begin{vmatrix} -M_1{\omega_{n_1}}^2 + Kl_1 & \chi_{11} \\ -M_2{\omega_{n_1}}^2 + Kl_2 & \chi_{21} \end{vmatrix} = 0 and \begin{vmatrix} -M_1{\omega_{n_2}}^2 + Kl_1 & \chi_{12} \\ -M_2{\omega_{n_2}}^2 + Kl_2 & \chi_{22} \end{vmatrix} = 0 \quad (15)$$

Table 1 Mechanical and geometrical properties of the ring and the support beams

Parameter	Value
l_s	150 µm
R_o	190 µm
R	40 µm
R_{in}	20 µm
h	20 µm
E	112.4 GPa
t_s	2 µm
n_s	4
ρ	2330 kg/m^3

To describe the closeness of the excitation frequency Ω to the natural frequencies, the detuning parameter has been defined as, $\Omega = \omega_n + \varepsilon\sigma$ where σ represents the deviation of the excitation frequency from the natural frequency, assuming $A(T_1) = \frac{1}{2}a_1(T_1)e^{ib_1(T_1)}$ and $B(T_1) = \frac{1}{2}a_2(T_1)e^{ib_2(T_1)}$ and applying some simplifications the frequency response curves in the vicinity of the first two primary resonances are obtained.

3 Results and discussions

The geometric and mechanical properties of the studied model are given in Table 1.

In this analysis, we consider four distinct scenarios, each within the underdamped regime for the damping coefficient c_s.These scenarios are characterized by four different quality factors corresponding to the first two modes, as illustrated in Fig. 2. Due to the nonlinear stiffness terms, sweeping the excitation frequency ω in the super harmonic regime reveals various resonance zones. The locations of these resonance zones on the frequency axis depend on both the amplitude of the base excitation and the quality factor. The frequency response curves corresponding to the super harmonic regime associated with the first two modes are illustrated below. It is worth mentioning that the amplitude of the base excitation has been assumed to vary i.e. $(\frac{\theta_0}{\omega^2})$ such that by increasing the excitation frequency the acceleration $\ddot{\theta}$ amplitude remains constant.

Due to the sources of nonlinearity, prior to the primary resonance, the system exhibits two super harmoni resonaces one in the vicinity of $\omega = 0.2$ (equal to $\Omega = 35.6$ kHz) and another one in the vicinity of $\omega = 0.35$ (equal to $\Omega =$ 62.4 kHz). It is noteworthy that these resonance zones are substantial because they exhibit high-amplitude motion, which is particularly significant in low-frequency resonators. This is crucial in the design of low-frequency MEMS resonators, as these devices are inherently associated with high resonance frequencies. While high resonance frequencies offer enhanced sensitivity, they also come with certain drawbacks that must be considered. In order to investigate the source of each superharmonic resonance zone, we have considered two frequencies, ω=0.2 and ω=0.5 (equal to $\Omega = 89.12$ kHz), both below the primary resonance. Figure 3 depicts the frequency content of both modes for each individual case, with the associated steady-state time response and the phase plane indicated as insets $(g = 10^{-6}\text{m}, \theta_0 = \frac{\pi}{10}\text{ rad})$.

As illustrated, assuming the excitation frequency in both cases to be x, the frequency content of the response includes odd multiples of the excitation frequency, i.e., 3x, 5x, 7x,

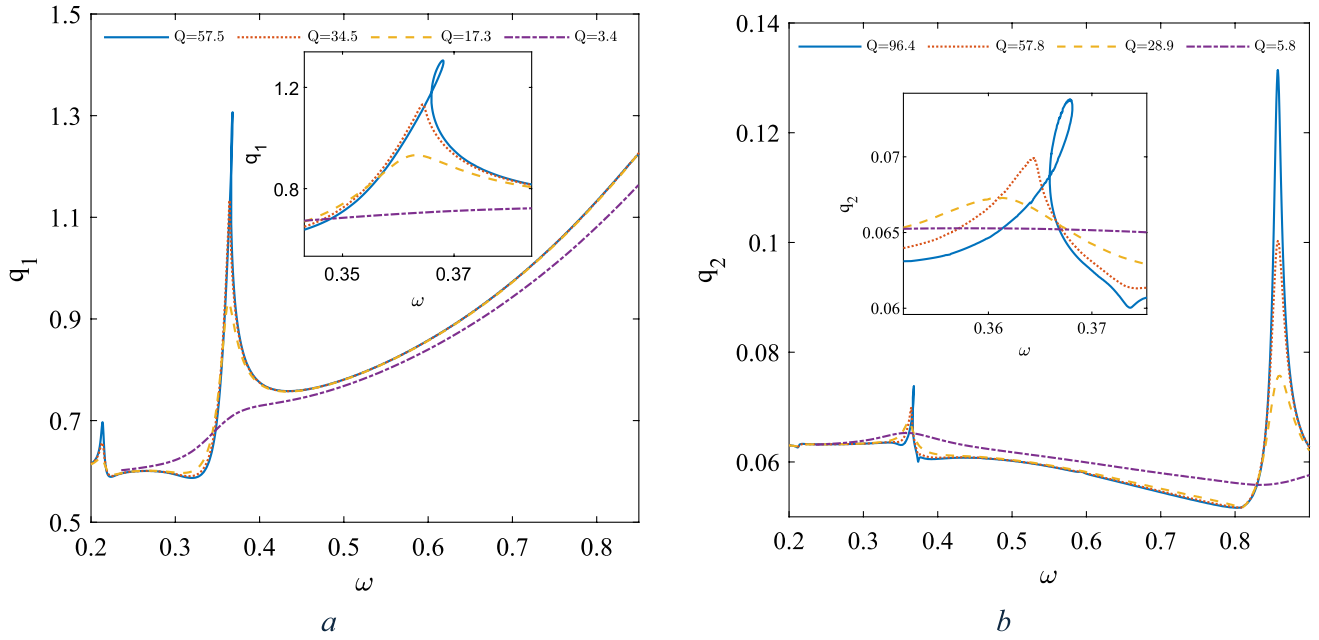

Fig. 2 The frequency response curve in the super harmonic resonance zone, **a** amplitude of first mode, **b** amplitude of the second mode $g = 10^{-6}m, \theta_0 = \frac{\pi}{10}rad$

and so on. This means that the system may be assumed as a function which gives off the odd multiples of the excitation frequency in the response and according any odd fraction i.e. $\frac{\omega_n}{x}$ of the primary resonance can be assummed as a superharmonic resonance zone. Given that the first primary resonance is in the vicinity of $\omega = 1.0$, the presence of the term $5\times$ maps the excitation frequency to the primary resonance. Consequently, a superharmonic resonance zone appears in the vicinity of $\frac{\omega_n}{5}$, which indirectly excites the primary resonance and is accordingly known as a superharmonic secondary resonance. The same rational can be applied to justify the presence of the remaining superharmonic resonance zones which are due to the 5x, $7\times$ and so on.

Figure 4, illustrates the frequency resonances in the vicinity of the first two non-dimensional primary resonances. Comparing the amplitude of each individual mode with that of the superharmonic ones depicted in Fig. 2, reveals that the amplitudes in this zone are considerable higher.

As shown in Fig. 4, sweeping the frequency in forward direction the generalised amplitude associated with both two modes increase and bend rightward which is due to the hardening nature of the response in the vicinity of both modes. The catastrophic cyclic fold bifurcation (CF) which is immediately followed by a jump, offeres a potential mechnisim of measuring the added mass to the central ring. The results have been derived for four different damping coefficients. As the quality factor increases (indicating a decrease in the damping coefficient), the generalized amplitude also increases. Figure 5 illustrates the frequency response curves associated with the first two modes obtained by both continuation and MTS methods. To ensure that the conditions for the magnitude ordering of the terms in Eq. (9) are met, we have assumed the nondimensionalizing parameters$g = 10^{-5}\mathrm{m}, \Theta = \frac{\pi}{100}\mathrm{rad}$. This adjustment is intended to reduce the order of magnitude of the nonlinear terms and the excitation terms to the order ofε. The results are obtained for three different damping coefficients asssociated with three different quality factors (Q) for each of the modes.

As illustrated in Fig. 5, the increase in the amplitude of the motion and deviation from the natural frequency no longer keeps either the nonlinear terms or the detuning parameter σ in the order of ε. Consequently, the results of the two methods deviate; however, given that the perturbation conditions are satisfied in the vicinity of the frequency ω_n, there exists substantial agreement between the continuation and MTS methods. Figure 6 shows the force response curve for associated with both of the modes and for two different conditions $\omega = 0.2$ and $\omega = 0.35$.

Associated with both excitation frequencies, as the amplitude of the excitation increases, the generalized amplitude of both modes also increases. This behavior is independent of the quality factor. However, as the generalized amplitude of each mode reaches a particular value, the system undergoes a local extremum, after which the amplitude relaxes within a certain range of the force amplitude until the system resumes its increasing behavior. Figure 7a, b depict the frequency response curves with two different masses of the

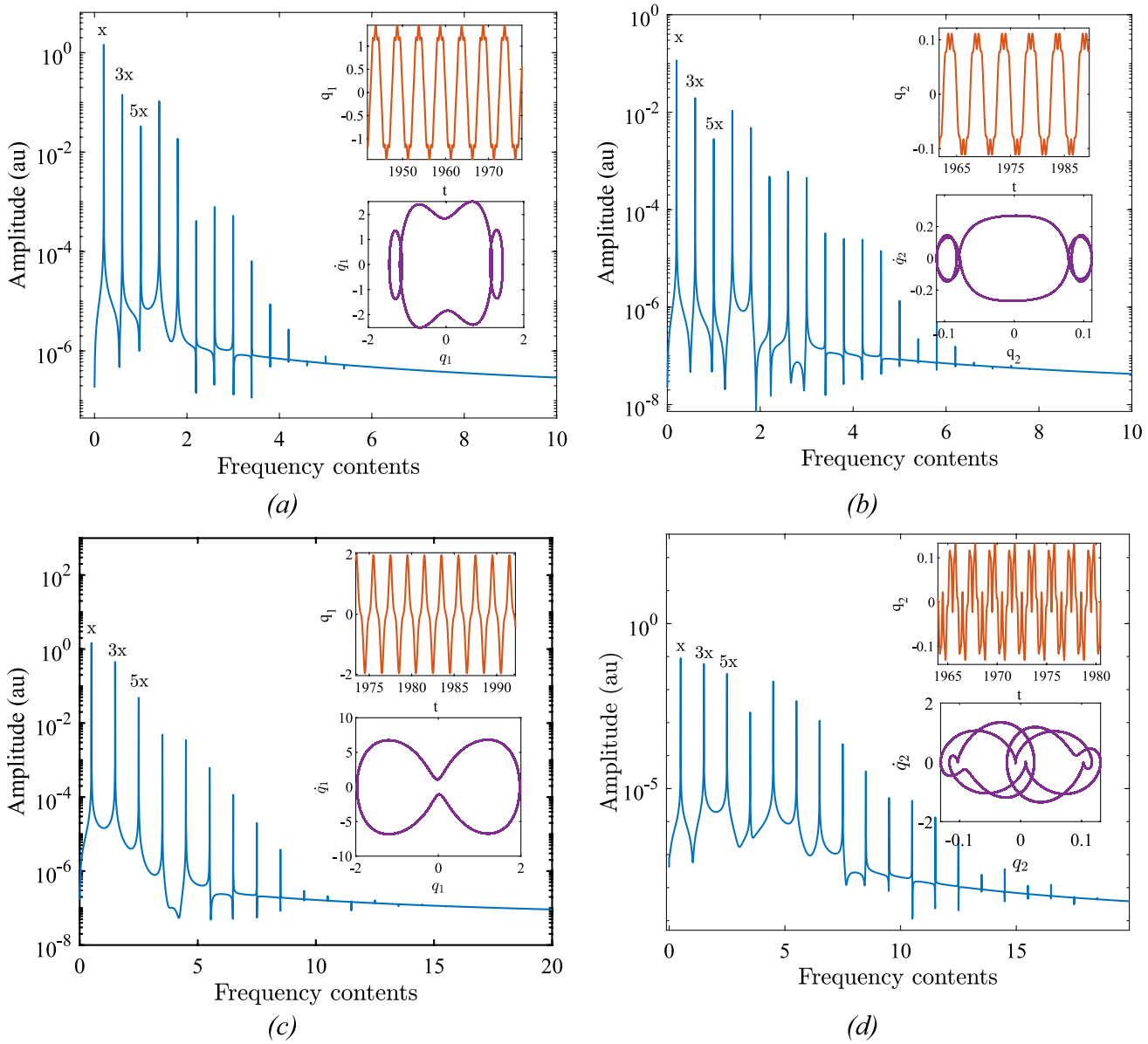

Fig. 3 Frequency contents of the response for two different cases: **a**, **b**: $\omega = 0.2$**c**, **d**: $\omega = 0.5,\ \mathrm{g} = 10^{-6}$ m , $\theta_0 = \frac{\pi}{10}$ rad

central ring, differing by 17 pg. As shown, with a mass difference of 17 pg, the shift of the peak points of the first two primary resonances are 10 Hz and 7 Hz, for two different quality factors of the first mode respectively; this frequency shift is associated with 0.58 pg/Hz. Figure 7c presents the linear frequency response curves for two different Q factors, alongside the evaluation of the natural frequencies obtained through COMSOL simulations.

As shown, the higher quality factor from which the in-plane resonators benefit leads to better sensitivity of the device to the mass difference of the central ring. The linear frequency response curve (neglecting the nonlinear terms) has been illustrated in Fig. 7c for thwo different Q factors. Finite element analysis is also carried out in COMSOL to verify the linear natural frequencies which there is a very good agreement. Furthermore the frequency shift due to the added mass both in nonlinear and linear modelling is examined. In the nonlinear analysis the sensitivity is 0.58 Hz/ pg whereas in linear analysis it was 0.5 Hz/ pg eqivelent to 16% impovement of the sensitivity.

4 Conclusion

In this paper, we investigated the dynamics of a micro-ring supported by four clamped beams and subjected to harmonic base excitation. The equations of motion were derived based on the discretization of the Lagrangian,

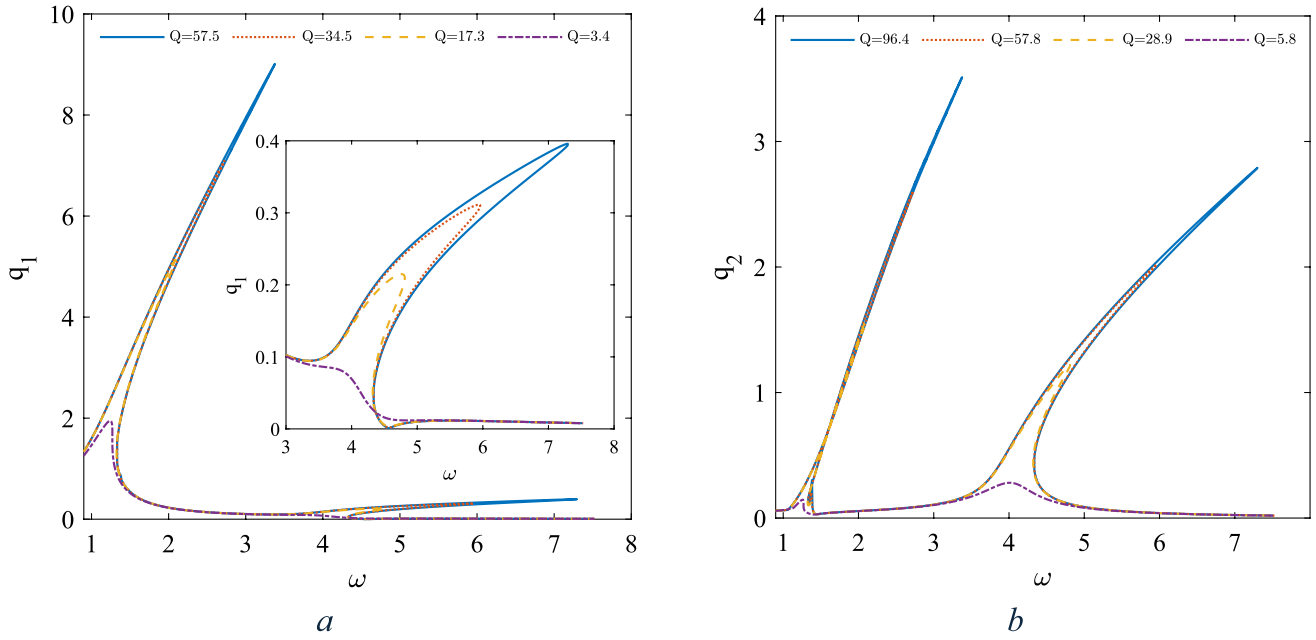

Fig. 4 The frequency response curve in the vicinity of the first two natural frequencies, **a** amplitude of first mode, **b** amplitude of the second mode

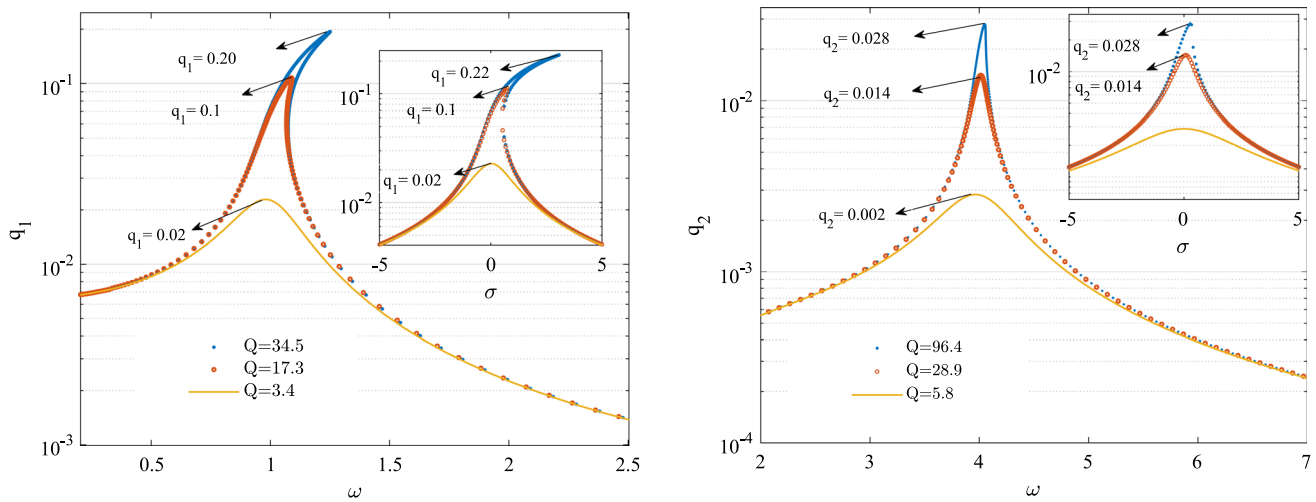

Fig. 5 Frequency response curves in the vicinity of the primary resonance based on continuation method and MTS method as inset, **a** amplitude of the first mode, **b** amplitude of the second mode

resulting in a reduced-order model. Frequency response curves were obtained using the continuation method and verified using the Method of Multiple Scales (MTS), ensuring the terms were balanced according to the governing equations. Our analysis revealed that as the amplitude of the excitation increases, the results of the perturbation and continuation methods diverge, attributed to the disruption in the balancing of the terms' magnitudes. Frequency response curves were derived for both the super harmonic regime and primary resonances. To identify the sources of specific super harmonic resonances, we examined the frequency content of the response for two different excitation frequencies. This analysis revealed that the amplitude contains odd multiples of the excitation frequency, leading to super harmonic resonance in the regions $\frac{\omega_n}{2n+1}$, where n is a natural number. The effect of the quality factor on the motion amplitudes and the frequency response curves was also examined. To investigate the primary resonance based on the perturbation

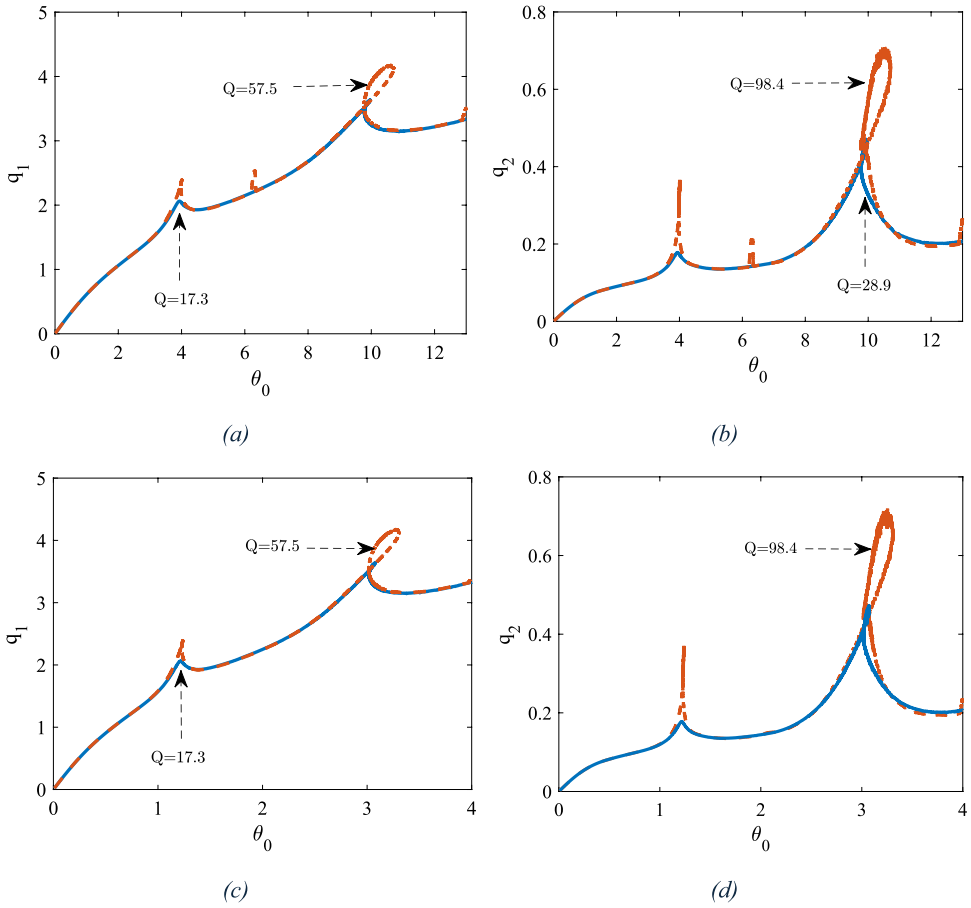

Fig. 6 Force response curves of the generalised coordinates for two different excitation frequencies, **a**, **b**$\omega = 0.2$, **c**, **d**$\omega = 0.35$

technique we had to keep the amplitude of the excitation term small enough so that the harmonic excitation force appears not in the very first linear equation, as a result we were unable to compare the two methods for higher amplitudes of the motion. The frequency response curves in the vicinity of primary resonances exhibited a hardening response as they bent rightward on the frequency domain; this was attributed to the type of the supporting beams. It was concluded that the mass difference 17 pg resulted in the measurable frequency shift equal to 10 and 7 Hz in the location of the bifurcation point on the frequency response curves; Besides the nonlinear analysis we carried out linear analysis to compare the effect of nonlinearity on the sensitivity; it was concluded that the sensitivity improves 16% in nonlinear regime. The results of the study are promising in developing and improving the sensitivity and quality factor of MEMS resonators particularly for mass detection applications. Future studies will include the fabrication and testing of the proposed model, during which its mass-sensing capability will be demonstrated.

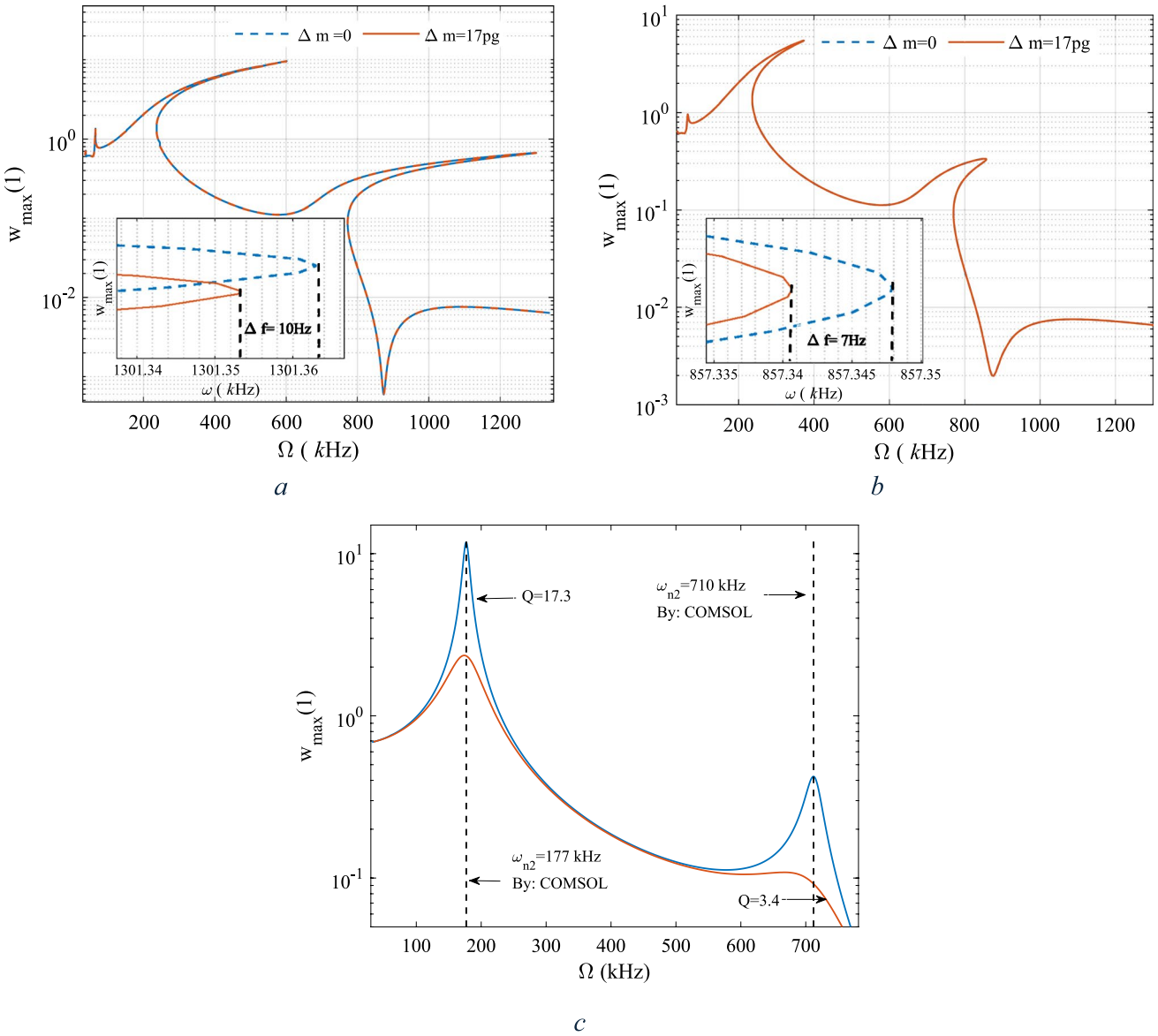

Fig. 7 The frequency response curve in the vicinity of the first two natural frequencies, nonlinear analysis **a** Q = 57.5, **b** Q = 17.3, **c** linear analysis

Appendix 1

Assuming a disc with radius R, connected to a beam with length l, (Fig. 8).

density ρ and young's modulus E, and deflection $w(x,t)$ in lateral direction, the kinetic (T) and the potential (U) energies will be in the following forms:

$$T = \frac{\rho A}{2} l \left(\frac{g}{T}\right)^2 \int_0^1 \dot{w}^2 l dx + \frac{1}{2} I_D \left(\frac{g}{lT}\right)^2$$
$$\dot{w}_x(1,t)^2, U = \frac{EI}{2} \left(\frac{g}{l^2}\right)^2 \int_0^1 w''^2 l dx \quad (16)$$

Non-dimensionalparameters$\widehat{x} = x/l, \widehat{w} = w/g, \widehat{t} = t/T$ have been substituted for x, w, and t respectively. For simplicity the hats have been dropped. Here l, g and T are non-dimensionalising parameters. In Eq. A-1, the rotation of the disc is approximated by the slope of the beam at the connection point to the disc, i.e.,$w_x(1,t) = \varphi$. Applying integration by parts, the variation of the Hamiltonian,

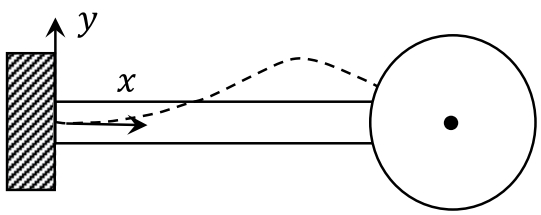

Fig. 8 Schematics of a disc with a pin at the centre connected to a clamped beam

$\delta\int_0^t H dt = 0$ (Nikpourian et al. 2020; Ghavami et al. 2022) has been set to zero.

$$\begin{aligned}\int_0^t \Bigg\{ \int_0^1 \Big(-\rho A l \left(\tfrac{g}{T}\right)^2 \ddot{w}\delta w - EI\tfrac{g^2}{l^3} w^{IV}\delta w \Big) dx \\ + \Big(-I_D \left(\tfrac{g}{Tl}\right)^2 \ddot{w}_x(1,t)\,\delta w_x(1,t) \\ -EI\tfrac{g^2}{l^3} w_{xx}\,\delta w_x\big|_0^1 + EI\tfrac{g^2}{l^3} w_{xxx}\,\delta w\big|_0^1 \Big) \Bigg\} dt \\ = 0\end{aligned} \tag{17}$$

Assuming $T^2 = \frac{\rho A l^4}{EI}$ the linear motion equation and the associated boundary conditions reduce to:

$$\ddot{w} + w^{IV} = 0$$

$$\begin{aligned}-I_D \left(\tfrac{g}{Tl}\right)^2 \ddot{w}_x(1,t)\,\delta w_x(1,t) - EI\tfrac{g^2}{l^3} w_{xx}(1,t)\,\delta w_x(1,t) \\ +EI\tfrac{g^2}{l^3} w_{xxx}(1,t)\,\delta w(1,t) + EI\tfrac{g^2}{l^3} w_{xx}(0,t)\,\delta w_x(0,t) \\ -EI\tfrac{g^2}{l^3} w_{xxx}(0,t)\,\delta w(0,t) = 0\end{aligned} \tag{18}$$

With the assumption $\delta w(1,t) = -\frac{R}{l}\delta w_x(1,t)$, the boundary condition terms in Eq. (18) reduce to:

$$I_D\left(\frac{g}{Tl}\right)^2 \ddot{w}_x(1,t)\,\frac{l}{R} + EI\frac{g^2}{l^3} w_{xxx}(1,t) + EI\frac{g^2}{l^3} w_{xx}(1,t)\,\frac{l}{R} = 0 \tag{19}$$

$$w(0,t) = 0, w_x(0,t) = 0, w(1,t) = -\frac{R}{l}$$

The first two shape functions which satisfy the boundary conditions specified in Eq. (19) have been derived as follows:

$$\begin{aligned}\psi_1(x) = 2.8743\sin(1.8958x) - 2.0588\cos(1.8958x) \\ -2.8743\sinh(1.8958x) + 2.0588\cosh(1.8958x)\end{aligned} \tag{20}$$

$$\begin{aligned}\psi_1(x) = 1.0015\sin(4.8111x) - 1.0177\cos(4.8111x) \\ -1.0015\sinh(4.8111x) + 1.0177\cosh(1.8958x)\end{aligned}$$

Appendix 2

The coefficients of the terms in Eq. (8) are as follows:

$M_1 = 2\alpha_{111} + 2\alpha_{211}$	$M_2 = \alpha_{121} + \alpha_{221} + \alpha_{112} + \alpha_{212}$
$Kl_1 = 2\beta_{111} - 2\Gamma_{1_{11}}$	$Kl_2 = \beta_{121} + \beta_{112} - \Gamma_{1_{21}} - \Gamma_{1_{12}}$
$Kn_1 = 4\beta_{21111}$	$Kn_2 = \beta_{22221} + \beta_{22212} + \beta_{22122} + \beta_{21222}$
$C_1 = 2\gamma_{11}$	$Kg_1 = 2\beta_{21221} + 2\beta_{22112} + 2\beta_{21212} + 2\beta_{22211} + 2\beta_{21122} + 2\beta_{22121}$
$C_2 = \gamma_{12} + \gamma_{21}$	
$F_1 = -\dot{\Gamma}_{2_1} - \dot{\Gamma}_{3_1}$	$Kg_2 = 3\beta_{21112} + 3\beta_{22111} + 3\beta_{21211} + 3\beta_{21121}$
$M_3 = 2\alpha_{122} + 2\alpha_{222}$	
$Kl_3 = 2\beta_{122} - 2\Gamma_{1_{22}}$	$Kn_4 = 4\beta_{22222}$
$Kn_3 = \beta_{21112} + \beta_{22111} + \beta_{21211} + \beta_{21121}$	
$C_3 = 2\gamma_{22}$	$Kg_3 = 3\beta_{22122} + 3\beta_{21222} + 3\beta_{22221} + 3\beta_{22212}$
$F_2 = -\dot{\Gamma}_{2_2} - \dot{\Gamma}_{3_2}$	$Kg_4 = 2\beta_{21212} + 2\beta_{22121} + 2\beta_{21212} + 2\beta_{22211} + 2\beta_{21122} + 2\beta_{22112}$

where:

$\alpha_{1ij} = \frac{1}{2} n_s (\rho A)_s \frac{g^2 l_s}{T^2} \int_0^1 \psi_{s_i}(x_s)\,\psi_{s_j}(x_s)\,dx_s$	$\gamma_{ij} = \frac{1}{2} n_s c_s \frac{g^2 l_s}{T^2} \int_0^1 \psi_{s_i}(x_s)\,\psi_{s_j}(x_s)\,dx_s$
$\alpha_{2ij} = \frac{1}{2} I_D \frac{g^2}{l_s^2 T^2} \psi'_{s_i}(1)\,\psi'_{s_j}(1)$	$\Gamma_{1_{ij}} = \frac{1}{2} n_s (\rho A)_s \dot{\theta}^2 \frac{\Theta^2 g^2 l_s}{T^2} \int_0^1 \psi_{s_i}(x_s)\psi_{s_j}(x_s)dx_s$
$\beta_{1_{ij}} = \frac{1}{2} n_s (EI)_s \frac{g^2}{l_s^3} \int_0^1 \psi''_{s_i}(x_s)\,\psi''_{s_j}(x_s)\,dx_s$	
$\Gamma_{2_i} = -n_s (\rho A)_s \dot{\theta} \frac{\Theta g l_s}{T^2} \int_0^1 (R_o - l_s x_s)\,\psi_{s_i}(x_s) dx_s$	$\Gamma_{3i} = I_D \dot{\theta} \frac{\Theta g}{T^2 l_s} \psi'_{s_i}(1)$
$\beta_{2_{ijko}} = \frac{EA}{8} \frac{g^4}{l_s^3} n_s \int_0^1 \psi'_{s_i}(x_s)\,\psi'_{s_j}(x_s)\,dx_s \int_0^1 \psi'_{s_k}(x_s)\,\psi'_{s_o}(x_s)\,dx_s$	

Acknowledgements This research was supported by the Engineering and Physical Sciences Research Council (EPSRC) under Grant No. EP/Y027914/1. We acknowledge the EPSRC's support in enabling this work, which addresses key challenges design and fabrication of super sensitive MEMS mass sensors.

Author contributions S.A. Did the modelling, simulation and analysis H.M. Reviewed the paper H.H.KH. Reviewed the paper P.S. Reviewd the paper and helped with Comsol modelling M. I. Y. Reviewed the paper Gh. R. Reviewed the Paper and helped with mathematical modelling.

Funding This work was supported by Engineering and Physical Sciences Research Council, EP/Y027914/1.

Data availability No datasets were generated or analysed during the current study.

Declarations

Conflict of interest The authors declare no competing interests.

References

Alneamy AM, Ouakad HM (2023) Inertia mass bio-sensors based on snap-through phenomena in electrostatic MEMS shallow arch resonators. Int J Mech Sci 238:107825

Alvarez M, Lechuga LM (2010) Microcantilever-based platforms as biosensing tools. Analyst 135(5):827–836

Azizi S et al (2012) Dynamics of micro-rotational disk mass sensor structures: characterization and sensitivity analysis in Cornell nanoscale science & technology facility 35th anniversary celebration & annual meeting. Ithaca, New York

Azizi S et al (2014) Tuning the primary resonances of a micro resonator, using piezoelectric actuation. Nonlinear Dyn 76(1):839–852

Azizi S, Rezaei Kivi A, Marzbanrad J (2017) Mass detection based on pure parametric excitation of a micro beam actuated by piezoelectric layers. Microsyst Technol 23(4):991–998

Azizi S et al (2022) Bifurcation analysis and nonlinear dynamics of a capacitive energy harvester in the vicinity of the primary and secondary resonances. Nonlinear Dyn 108(2):873–886

Azizi S et al (2023) On the nonlinear dynamics of a piezoresistive based mass switch based on catastrophic bifurcation. Int J Mech Mater des 19(3):521–535

Baguet S et al (2019) Nonlinear dynamics of micromechanical resonator arrays for mass sensing. Nonlinear Dyn 95(2):1203–1220

Botamanenko DY et al (2023) Electrostatic linear ion trap optimization strategy for high resolution charge detection mass spectrometry. J Am Soc Mass Spectrom 34(8):1731–1740

Chauhan S, Ansari MZ (2021) Vacuum-assisted piezoelectric cantilever mass sensor performance. J Mech Sci Technol 35(12):5489–5494

Chellasivalingam M et al (2020) Weakly coupled piezoelectric MEMS resonators for aerosol sensing. Sensors (Basel, Switzerland) 20(11):3162

De Pasquale G, Somà A (2010) Dynamic identification of electrostatically actuated MEMS in the frequency domain. Mech Syst Signal Process 24(6):1621–1633

Elliott AG et al (2017) Single particle analyzer of mass: a charge detection mass spectrometer with a multi-detector electrostatic ion trap. Int J Mass Spectrom 414:45–55

Firoozy P, Khadem SE, Pourkiaee SM (2017) Broadband energy harvesting using nonlinear vibrations of a magnetopiezoelastic cantilever beam. Int J Eng Sci 111:113–133

Gfeller KY, Nugaeva N, Hegner M (2005) Micromechanical oscillators as rapid biosensor for the detection of active growth of Escherichia coli. Biosens Bioelectron 21(3):528–533

Ghavami M, Azizi S, Ghazavi MR (2022) Dynamics of a micro-cantilever for capacitive energy harvesting considering nonlinear inertia and curvature. J Braz Soc Mech Sci Eng 44(4):124

Gupta A, Singh TS, Yadava RDS (2018) MEMS sensor array-based electronic nose for breath analysis—a simulation study. J Breath Res 13(1):016003

Hansen KM, Thundat T (2005) Microcantilever biosensors. Methods 37(1):57–64

Hashoul D, Haick H (2019) Sensors for detecting pulmonary diseases from exhaled breath. Eur Respir Rev 28(152):190011

Jafari H et al (2017) Novel mass detection based on magnetic excitation in anti-resonance region. Microsyst Technol 23(5):1377–1383

Jingjing W et al (2016) Development of microcantilever sensors for liver cancer detection. Adv Cancer Prevent. https://doi.org/10.4172/2472-0429.1000103

Johnson BN, Mutharasan R (2012) Biosensing using dynamic-mode cantilever sensors: a review. Biosens Bioelectron 32(1):1–18

Joshi P et al (2019) Distributed MEMS mass-sensor based on piezoelectric resonant micro-cantilevers. J Microelectromech Syst 28(3):382–389

Katzis K et al (2022) Breaking barriers in emerging biomedical applications. Entropy. https://doi.org/10.3390/e24020226

Kumar V et al (2011) Linear and nonlinear mass sensing using piezoelectrically-actuated microcantilevers. MEMS Nanotechnol 1:57–65

Kumar V et al (2011) Bifurcation-based mass sensing using piezoelectrically-actuated microcantilevers. Appl Phys Lett. https://doi.org/10.1063/1.3574920

Kurmendra RK (2019) MEMS based cantilever biosensors for cancer detection using potential bio-markers present in VOCs: a survey. Microsyst Technol 25(9):3253–3267

Lee JH, Kim TS, Yoon KH (2004) Effect of mass and stress on resonant frequency shift of functionalized Pb(Zr0.52Ti0.48)O3 thin film microcantilever for the detection of C-reactive protein. Appl Phys Lett 84(16):3187–3189

Lee J et al (2011) Suspended microchannel resonators with piezoresistive sensors. Lab Chip 11(4):645–651

Li C et al (2019) Microcantilever array biosensor for simultaneous detection of carcinoembryonic antigens and α-fetoprotein based on real-time monitoring of the profile of cantilever. ACS Sens 4(11):3034–3041

Maraldo D, Mutharasan R (2007) Detection and confirmation of Staphylococcal Enterotoxin B in Apple juice and milk using

Piezoelectric-Excited Millimeter-Sized Cantilever sensors at 2.5 fg/mL. Anal Chem 79(20):7636–7643
Meesala VC, Hajj MR, Abdel-Rahman E (2020) Bifurcation-based MEMS mass sensors. Int J Mech Sci 180:105705
Mohammad IY (2011) MEMS linear and nonlinear statics and dynamics. Springer, Cham
Nayfeh PFP (2004) Linear and Nonlinear Structural Mechanics. Wiley-VCH, New York
Nayfeh AH, Balachandran B (2008) Applied nonlinear dynamics: analytical, computational, and experimental methods, 2nd edn. Wiley, New York
Nayfeh AH et al (2010) Nonlinear dynamics of a resonant gas sensor. Nonlinear Dyn 59(4):607–618
Nayfeh AH (1981) Introduction to Perturbation Techniques. Wiley, New York
Nikpourian A, Ghazavi MR, Azizi S (2020) Size-dependent modal interactions of a piezoelectrically laminated microarch resonator with 3:1 internal resonance. Appl Math Mech 41(10):1517–1538
Olcum S et al (2014) Weighing nanoparticles in solution at the attogram scale. Proc Natl Acad Sci U S A 111(4):1310–1315
Park K et al (2012) Resonant MEMS mass sensors for measurement of microdroplet evaporation. J Microelectromech Syst 21(3):702–711
Rashidi Z, Azizi S, Rahmani O (2023) Nonlinear dynamics of a piezoelectrically laminated initially curved microbeam resonator exposed to fringing-field electrostatic actuation. Nonlinear Dyn 111(22):20715–20733
Rashidi Z, Azizi S, Rahmani O (2024) Period-doubling cascade route to chaos in an initially curved microbeam resonator exposed to fringing-field electrostatic actuation. Nonlinear Dyn. https://doi.org/10.1007/s11071-024-09575-y
Shafiee H et al (2013) Acute on-chip HIV detection through label-free electrical sensing of viral nano-lysate. Small 9(15):2553–2563
Stachiv I et al (2020) Mass spectrometry of heavy analytes and large biological aggregates by monitoring changes in the quality factor of nanomechanical resonators in air. ACS Sens 5(7):2128–2135
Stachiv I et al (2022) Achievable accuracy of resonating nanomechanical systems for mass sensing of larger analytes in GDa range. Int J Mech Sci 224:107353
Timurdogan E et al (2011) MEMS biosensor for detection of Hepatitis A and C viruses in serum. Biosens Bioelectron 28(1):189–194
Toledo J et al (2019) Piezoelectric MEMS resonators for cigarette particle detection. Micromachines. https://doi.org/10.3390/mi10020145
Wang S et al (2015) A new device for liver cancer biomarker detection with high accuracy. Sens Bio-Sens Res 4:40–45
Xu J, Yan R, Chen J (2024) Piezoelectric Impedance-based robust mass sensing with temperature decoupling. In: Proceedings volume 12951, health monitoring of structural and biological systems XVIII. pp. 55.
Yaqoob U et al (2022) Selective multiple analyte detection using multi-mode excitation of a MEMS resonator. Sci Rep 12(1):5297
Yuksel M et al (2019) Nonlinear nanomechanical mass spectrometry at the single-nanoparticle level. Nano Lett 19(6):3583–3589
Zamanzadeh M, Ouakad HM, Azizi S (2020) Theoretical and experimental investigations of the primary and parametric resonances in repulsive force based MEMS actuators. Sens Actuators, A 303:111635